⑬ NW **LEVEL** Ⅱ
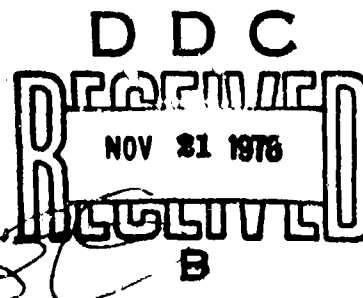
TECHNICAL REPORT ARLCD-TR-78017

FAILURE ANALYSIS OF THE LIGHTWEIGHT COMPANY MORTAR SYSTEM 60 MM MORTAR FIN

PAT CALELLA
JOEL SHAPPIRIO

D D C

RECEIVED

NOV 21 1978

B

SEPTEMBER 1978

US ARMY ARMAMENT RESEARCH AND DEVELOPMENT COMMAND
LARGE CALIBER
WEAPON SYSTEMS LABORATORY
DOVER, NEW JERSEY

DRDUCOM

78 10 17 056

REPORT DOCUMENTATION PAGE		READ INSTRUCTIONS BEFORE COMPLETING FORM
1. REPORT NUMBER Technical Report ARLCD-TR-78017	2. GOVT ACCESSION NO.	3. RECIPIENT'S CATALOG NUMBER
4. TITLE (and Subtitle) Failure Analysis of the Lightweight Company Mortar System 60 mm Mortar Fin		5. TYPE OF REPORT & PERIOD COVERED
		6. PERFORMING ORG. REPORT NUMBER
7. AUTHOR(s) Pat Calella Joel Shappirio		8. CONTRACT OR GRANT NUMBER(s)
9. PERFORMING ORGANIZATION NAME AND ADDRESS Commander, ARRADCOM Large Caliber Weapon Systems Laboratory Dover, NJ 07801		10. PROGRAM ELEMENT, PROJECT, TASK AREA & WORK UNIT NUMBERS
11. CONTROLLING OFFICE NAME AND ADDRESS Commander, ARRADCOM ATTN: DRDAR-TSS Dover, NJ 07801		12. REPORT DATE September 1978
		13. NUMBER OF PAGES 44
14. MONITORING AGENCY NAME & ADDRESS(if different from Controlling Office)		15. SECURITY CLASS. (of this report) Unclassified
		15a. DECLASSIFICATION/DOWNGRADING SCHEDULE

16. DISTRIBUTION STATEMENT (of this Report)

Approved for public release; distribution unlimited.

17. DISTRIBUTION STATEMENT (of the abstract entered in Block 20, if different from Report)

18. SUPPLEMENTARY NOTES

D D C

NOV 21 1978

B.

19. KEY WORDS (Continue on reverse side if necessary and identify by block number)

Mortar
Failure analysis
Electron probe
Microcrack

20. ABSTRACT (Continue on reverse side if necessary and identify by block number)

An investigation of the XM27 fin section was conducted to determine the failure mechanism associated with the longitudinal separation of the fins during test firings. The investigation implied that improper process controls during billet cooling resulted in microcracks, with high concentrations of magnesium and silicon in the area of the cracks. Upon extrusion, this defect was transferred to the extruded fin section resulting in fins which would not withstand the internal

20. Abstract (continued)

pressures attained during firing. Several recommendations are made to eliminate all defective fins from the final accepted parts.

ERRATA

Technical Report ARLCD-TR-78017

FAILURE ANALYSIS OF THE LIGHTWEIGHT
COMPANY MORTAR SYSTEM 60 MM MORTAR FIN

Pat Calella
Joel Shappirio

Pat Calella employed by the Large Caliber Weapon System Laboratory,
ARRADCOM, Dover, NJ. Joel Shappirio is an employee of the
Electronic Technology and Devices Laboratory, ERADCOM,
Ft. Monmouth, NJ.

ACKNOWLEDGMENT

TABLE OF CONTENTS

INTRODUCTION

The initial failure of an XM27 fin section occurred during a test firing at Aberdeen Proving Ground in December 1975 when the extruded fin separated longitudinally into two halves and failed to leave the launcher. Several additional malfunctions, similar in nature to the first, have occurred during test firings at Fort Benning, Fort Greely and Aberdeen Proving Grounds. A typical failed fin is shown in figure 1.

An investigation of the failure mechanism and mode was begun at Frankford Arsena' and Picatinny Arsenal, during which 1800 fins were subjected to mandrel tests resulting in another seven failures similar in nature to those experienced during test firing. A typical "normal" mandrel failure is shown in figure 2.

Examination of failed fin samples and comparison with "normal" mandrel ruptured samples were continued at Picatinny Arsenal and initiated at Fort Monmouth. The present report details the results of this investigation and outlines procedures which should lead to the elimination of the fin failure mode.

ALUMINUM PREPARATION AND EXTRUSION PROCESS

To form an ingot, the molten 6070 alloy is poured into a movable bottom mold. As the aluminum is poured, the movable bottom is lowered into a water bath and the ingots are allowed to cool before removal from the bath. These ingots, which have a nine-inch diameter, are then sliced into .9144 meter sections or billets. The face of each billet is subjected to a quick inspection by the saw operator who examines the billet faces for gross cracking. The billets are then heated in an open gas furnace until they reach a temperature of 538 to 552°C, placed on a conveyer belt leading to the extrusion press where they are extruded at a temperature between 524 to 552°C and finally cooled by water spray. Each billet yields an extruded length of approximately 24.4 meters at an extrusion rate of approximately 3 to 3.6 m/min. The flow pattern of the extruded billet causes the skin, which is high in magnesium and silicon oxides, to accumulate in the rear of the billet. Therefore, approximately 15 cm of the billet is cropped off after the extrusion is completed.
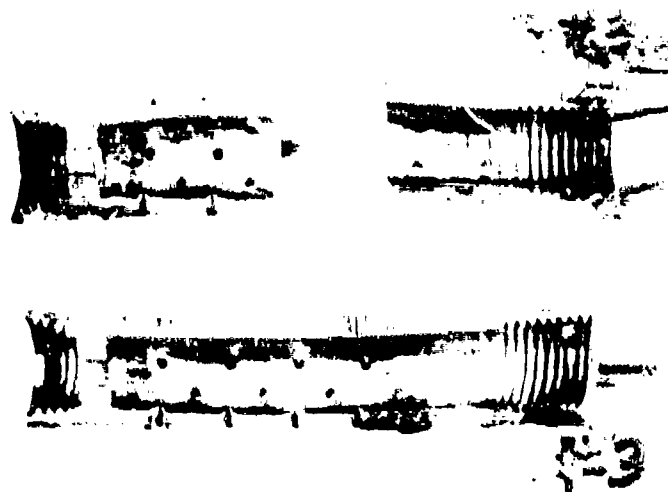
1

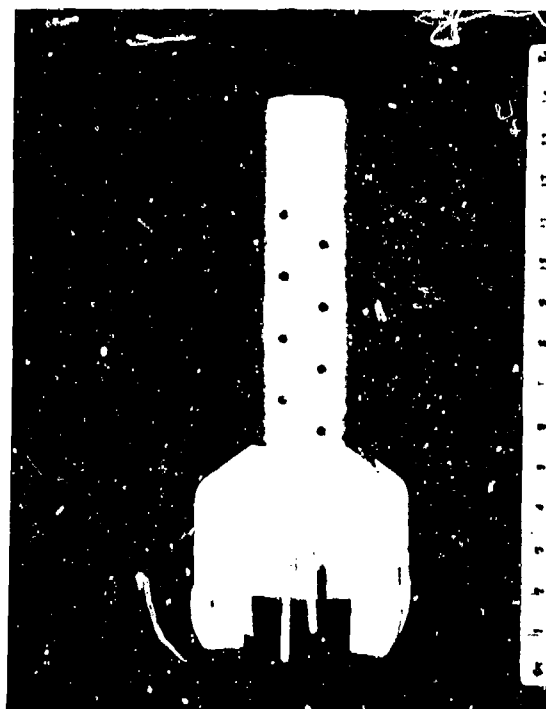Figure 1. Typical abnormal fin failure.

Figure 2. Typical normal fin failure.

A study of the flow patterns of similar extruded pieces shows that the face of the billet is extruded undisturbed. Therefore, cracks or voids near the face of the billet will remain in the extruded piece. Further down the billet, the flow pattern shows mixing. Therefore, defects not near the face of the billet will be mixed, strung out, and have no effect on the bulk property of the extruded material.

EXPERIMENTAL

Sample Preparation. Samples of fractured aluminum alloy 6070-T6 representing fins which failed normally during mandrel testing as well as abnormally failing samples from field testing were examined by light microscopy (LM), electron probe microanalysis (EP), and scanning electron microscopy (SEM). For SEM observation, fractured samples were examined directly without any sample preparation; in the case of the mandrel fracture, a cylindrical section of the fin body was removed by sawing and the section forced open for examination of the fracture surface. For EP and LM studies, standard metallographic polished sections were prepared. Selected samples were encapsulated in room temperature setting epoxy. Grinding was performed wet on silicon carbide papers ranging sequentially from 220 through 600 grit. Polishing was completed using 15, 7, 3, 1 and 0.25 μm diamond paste on paper, with final polishing using γ - alumina. Following each grinding and polishing step, the samples were ultrasonically cleaned in detergent and then rinsed in alcohol.

Light and Scanning Electron Microscopy. Cross-sections of normal and failed fin material were prepared for metallographic examination. Light microscope examination of these samples showed microstructures typical of 6070-T6 aluminum alloy with the presence, as expected, of abundant precipitate-phase inclusions. The only significant difference observed between failed and normal samples was a roughly linear defect which extended almost entirely across each of the sections of the failed fins. From light microscope examination, even at high magnification, it was not clear whether this defect represented the alignment of precipitate particles or some other linear defect present in the failed material. In order to investigate the feature in more detail, several areas of interest along the defect were indented to facilitate subsequent location in the SEM.

Figures 3A, B, and C are scanning electron micrographs showing the linear defect at magnifications of 140x, 1390x, and 3530x, respectively. In the low magnification view, the abundant precipitate phase particles show clearly; in addition, the location indents may also be seen. At higher magnifications, the defect is seen to be virtually continuous across the field of view, a continuity which, if due to the alignment of precipitate phase particles, would require a higher local concentration of such particles than is typical of other parts of even the failed alloy. In the higher magnification images, it may be observed that the precipitate particles exhibit either bright or dark contrast against the aluminum matrix, the higher secondary electron emission apparently related to the particle composition. (Brightness or darkness of the central parts of the precipitate phase particles are referred to here rather than contrast due to edge effects which has a different origin.) Those showing bright contrast appear to lie either at the same level or slightly higher than the aluminum matrix, those with darker contrast appear to lie at the same level or lower. It is clear from the photomicrographs that the linear defect has a much greater depth than even the more deeply eroded, or dark, precipitate phase. Measurements from SEM stereo pairs suggest a depth of approximately 1.5 μm for this defect. In addition, it is evident that any material removed by polishing has not been retained since no debris is evident at the bottom of the defect.

A fracture surface, similar to the one shown in figure 1, was examined utilizing the scanning electron microscope Figures 4A and 4B show the normal fracture and the failure fracture, respectively, at approximately 140x. The normal fracture shows the dimpling expected in a material such as this, while the failure fracture shows the striated fracture of the failure mode. As can be seen in figure 4B, an area of normal dimpled fracture exists along the lower portion of the failure fracture. The coexistence of both dimpled and striated fracture on the same surface is dramatically illustrated in figure 5. Figures 6A, 7A, and 8A show the normal fracture mode at approximately 340x, 650x, and 1300x, respectively. Figure 6B, 7B, and 8B show the failed fracture mode at approximately the same magnifications as the normal fracture series. Comparing the failed series with that of its normal counterparts, it is apparent that the resolution of the normal series is greater. Charging problems encountered while photographing the failed fracture surface indicate that the failed surface is comprised of a material which has lower conductivity than the normal fracture.

Figure 3A. Scanning electron micrograph showing a linear defect at 140x.
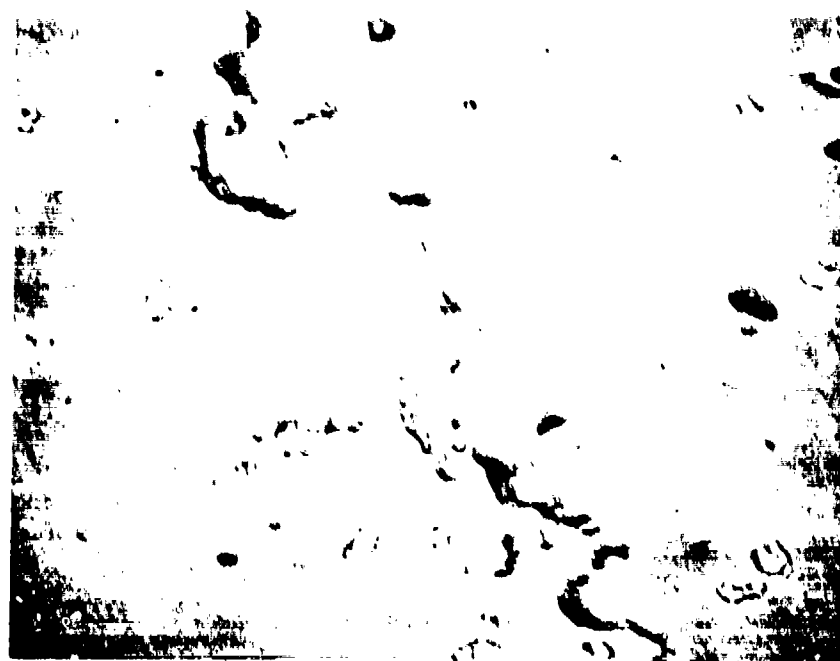
Rat 90

Figure 3B. Scanning electron micrograph showing a linear defect at 1390x.

5

Figure 3C. Scanning electron micrograph showing a linear defect at 3530x.

Figure 4A. Scanning electron micrograph showing a normal fracture at 140x.

Figure 4B. Scanning electron micrograph showing an abnormal fracture at 140x.
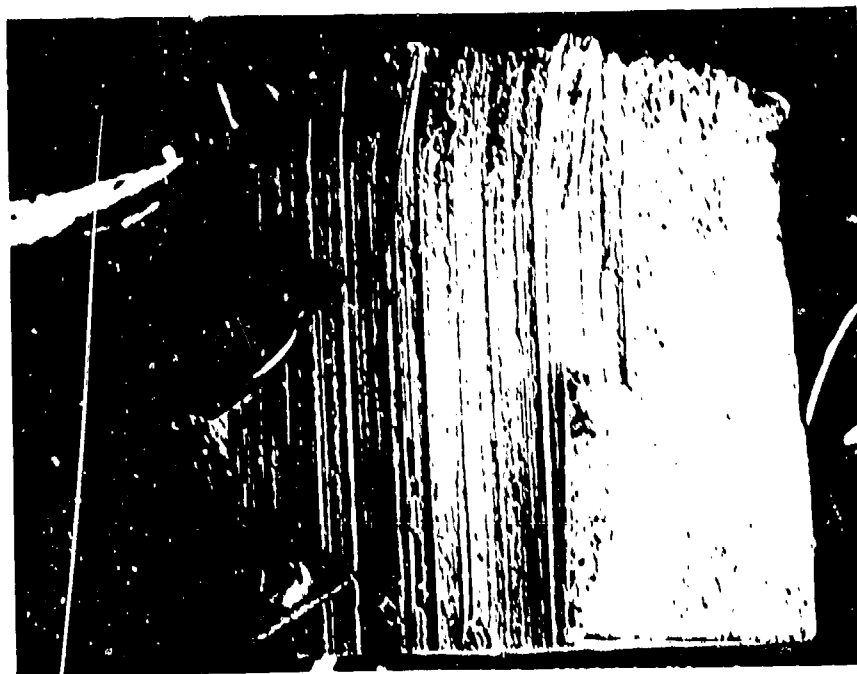
Figure 5. Scanning electron micrograph showing coexistence of both dimpled and striated fracture on the same surface.

Figure 6A. Scanning electron micrograph showing normal fracture at 340x.

Figure 6B. Scanning electron micrograph showing abnormal fracture at 340x.

9

45°

2622-2
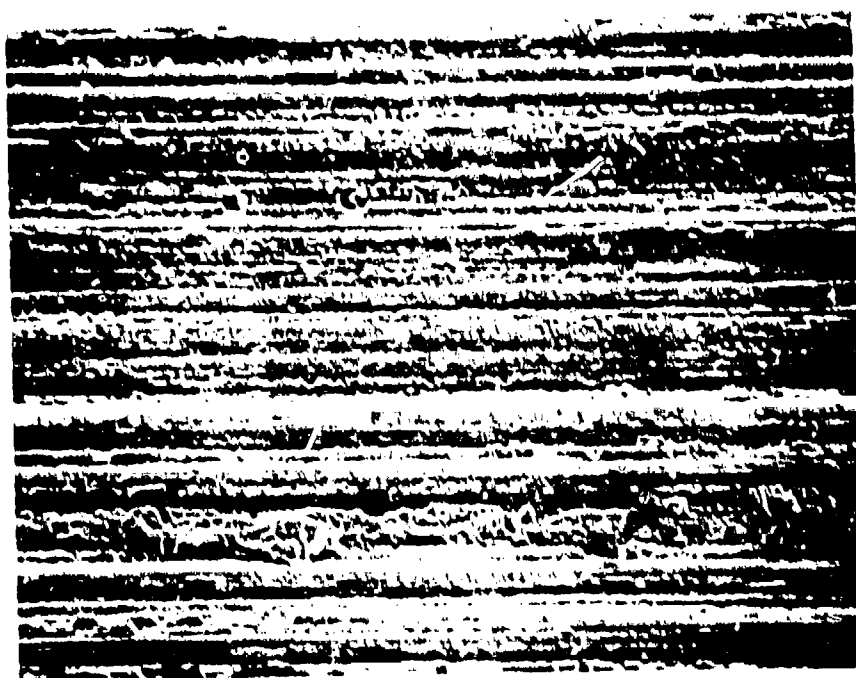
Figure 7A. Scanning electron micrograph showing normal fracture at 650x.

45°

2623-3

Figure 7B. Scanning electron micrograph showing abnormal fracture at 650x.

10

Figure 8A. Scanning electron micrograph showing normal fracture at 1300x.

Figure 8B. Scanning electron micrograph showing abnormal fracture at 1300 x.

11

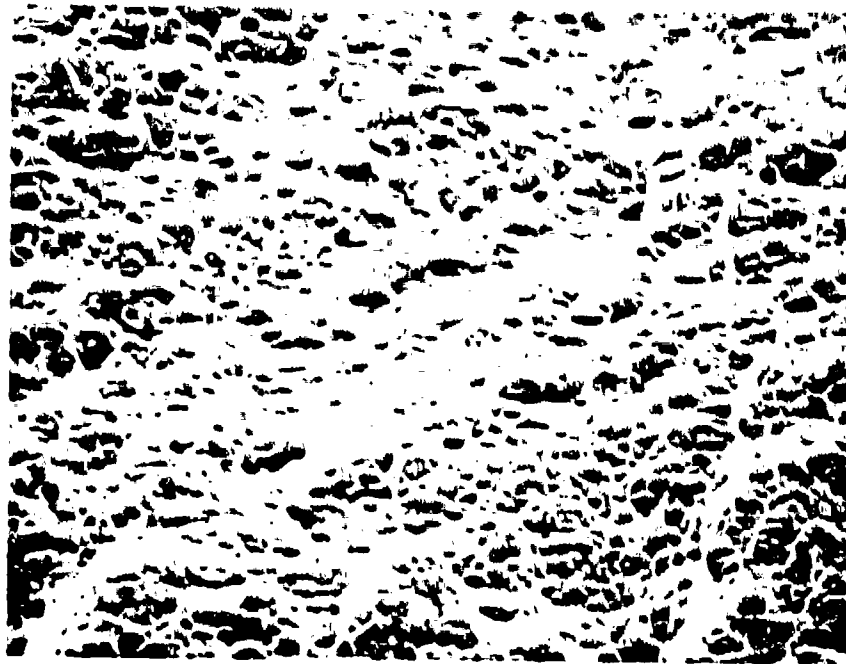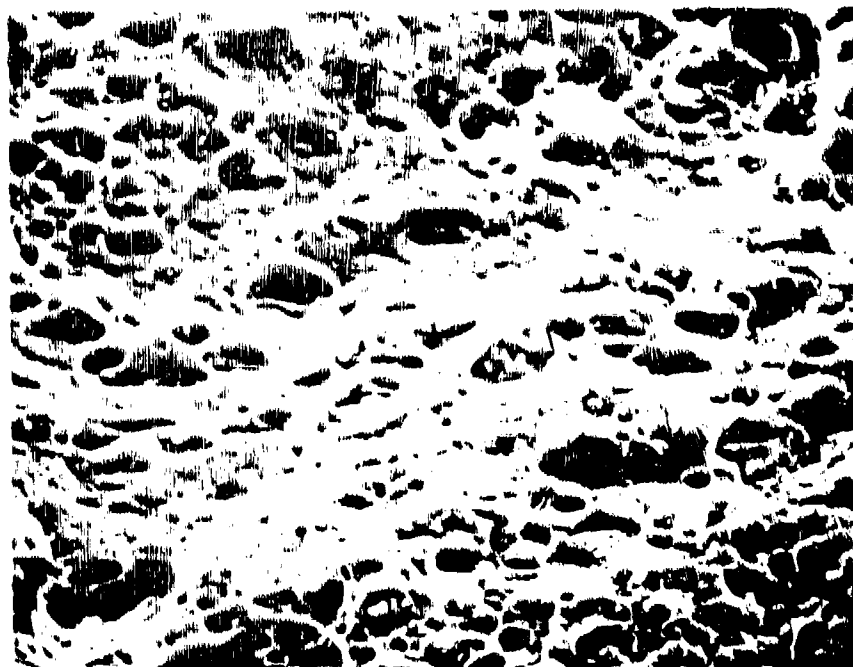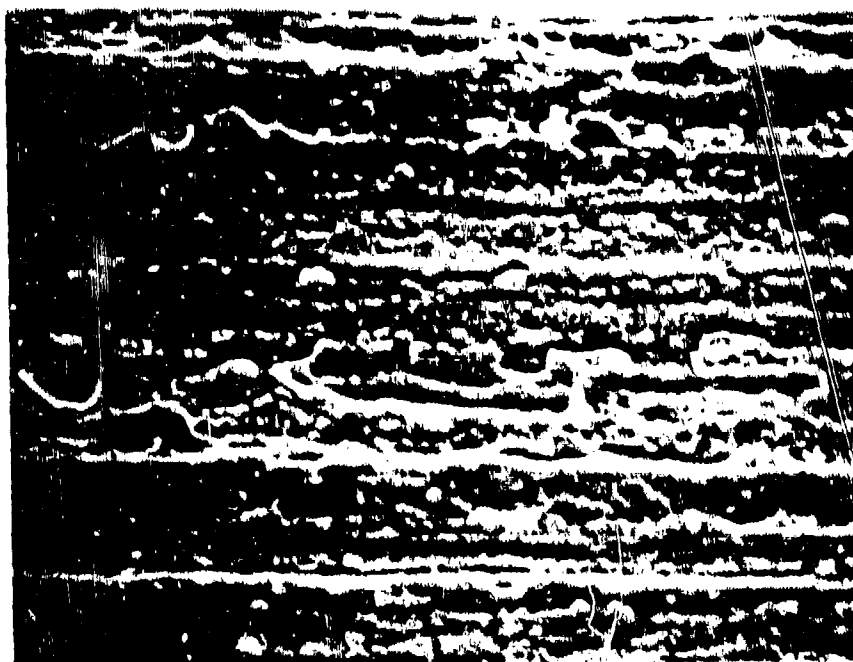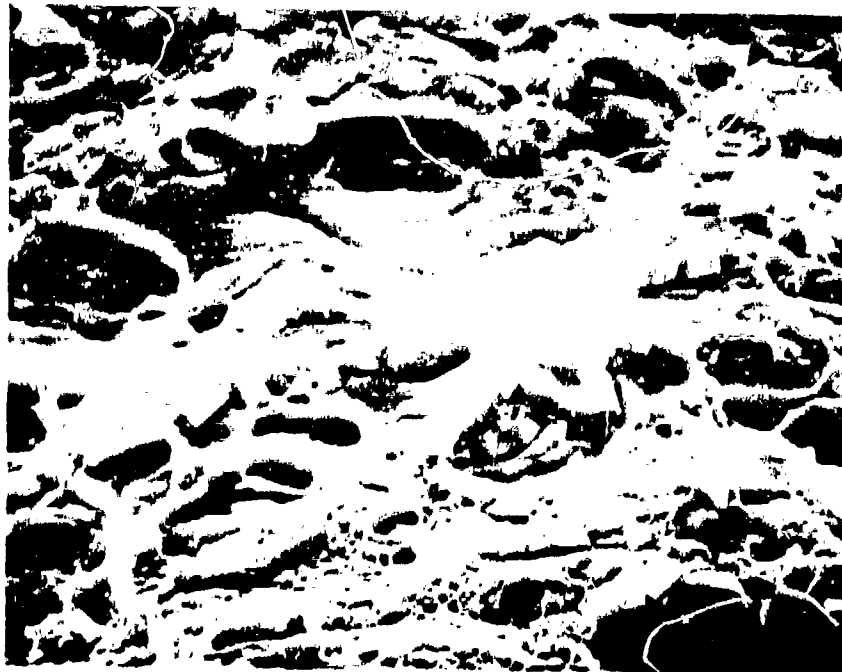Electron Probe Microanalysis. Electron probe methods were extremely useful in elucidating the mechanisms contributing to failure of the XM27 fins (an explanation of the operation of an electron probe for quantitative and qualitative analysis and for the production of x-ray scanning images show- ing images having two-dimensional element distribution on a sample surface is given in the appendix).

The first sample examined was the flat surface of the bulkhead from a failed fin (sample FA #1). The sample showed a linear defect extending almost entirely across the bulkhead surface. Figures 9A-F show electron probe scanning images for sample current, Al , Si, Mg, Mn, and Fe, respectively, at a magnification of 500x taken from a region of the bulk- head sample some distance from the crack. The scans are typical of normal 6070-T6 alloy. Note that although Al is rather homogeneously distributed across the alloy, the other elements are located at specific points on the alloy surface. These localized points represent second phase precipitates in the alloy. There is almost a direct one-to-one correspondence in dis- tribution of Mg and Si; these points correspond to the second phase Mg_2Si. In addition, there is a similarity in distribution of Fe and Mn; these locations probably correspond to the second phase (Fe, Mn) Al_6 .

Figures 10A-E (1000x) show the same bulkhead samples as figures 9A-F, but in the region of the linear defect observed on the surface. This linear feature shows clearly on the sample current image (fig. 10A). A homogeneous Al distribution is apparent again in the Al scan (fig. 10B) but note its apparent absence in the defect. The Mg (fig. 10C) and Si (fig. 10D) scans show a bimodal distribution of the two elements, one normal and similar to that observed in figure 9C (Si) and 9D (Mg). In addition, however, there is a strong local concentration of Mg and Si at the same location as the defect. Finally, the oxygen scan (fig. 10E) con- firms that the Mg and Si are present as oxides in the defect zone.

Figure 11, taken in the same and adjacent regions as figure 10A-E, is a montage of sample current and Mg x-ray images taken along the defect for a distance of approximately 43 μm. Note the almost continuous Mg segregation along this distance.

This series of probe scans demonstrates that a linear defect (in two dimensions) exists in the failed fin sample which could contribute to the failure of the round. The question then arises as to what information can be obtained to assess the extent of this defect in three dimensions. Accordingly, the fractured and separated surface of an alloy ring (SEM

12

764　　Disc　　Solid　　20µ
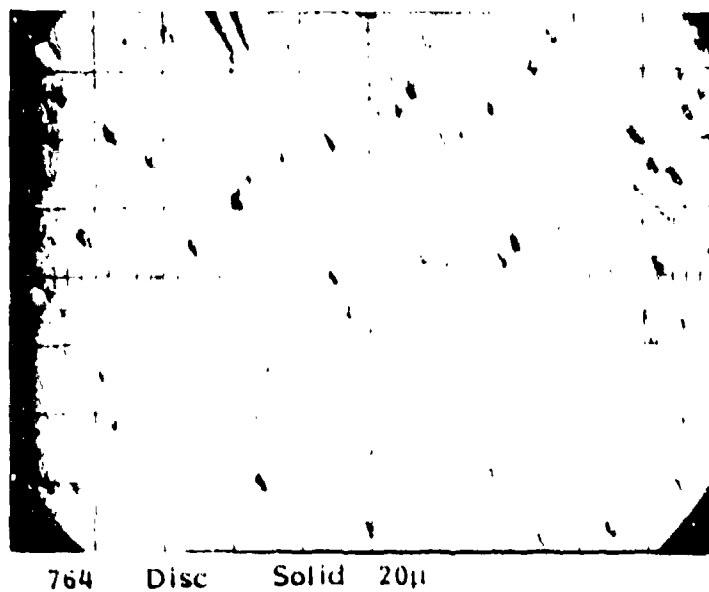
Figure 9A. Electron probe sample current scan showing a normal surface at 500x.

764　　Scan　Al Kα　Solid　20µ
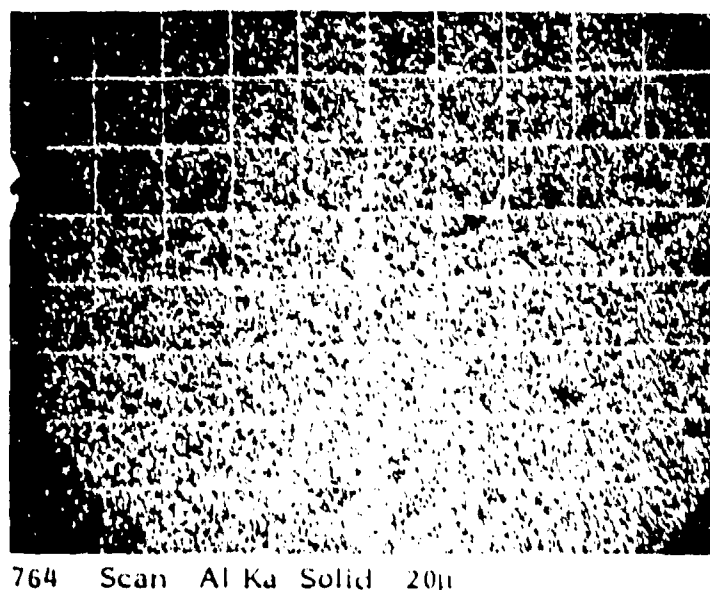
Figure 9B. Electron probe Al scan of the area shown in figure 9A.

13
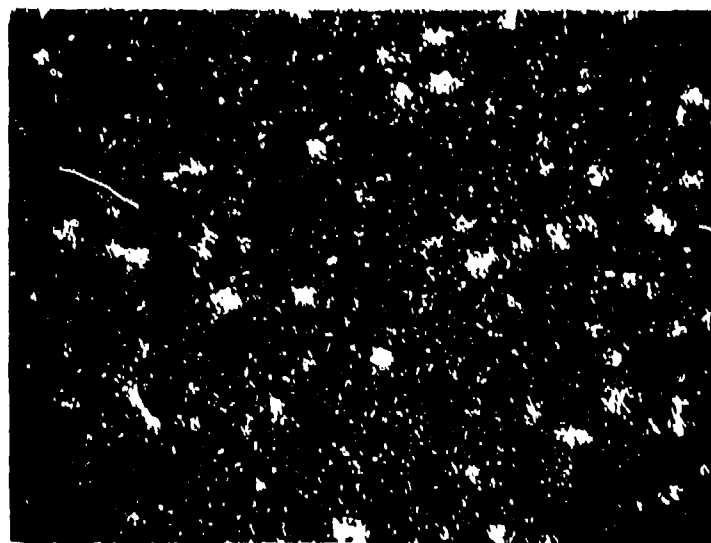
764   Scan   Si Kα   Solid   20µ

Figure 9C. Electron probe Si scan of the area shown in figure 9A.
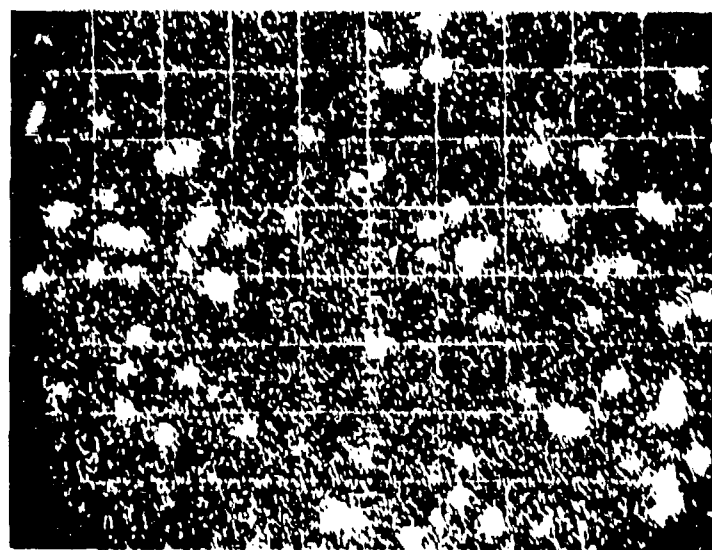
764   Scan   MG Kα   Solid   20µ

Figure 9D. Electron probe Mg scan of the area shown in figure 9A.

14
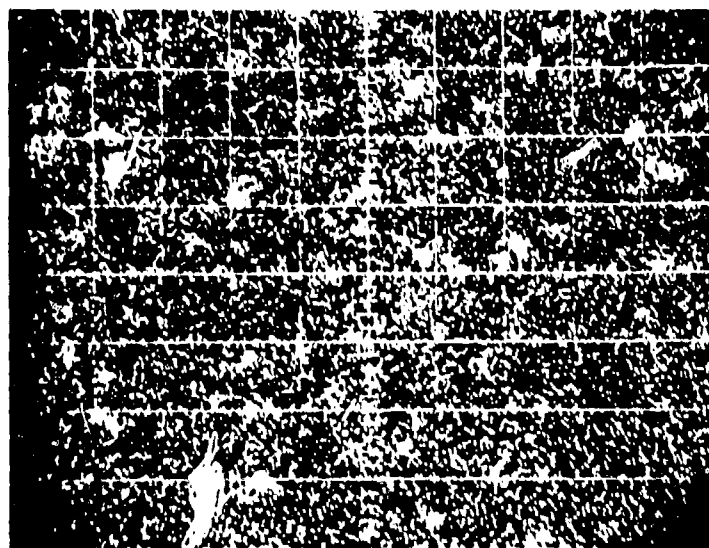
764   Scan   Mn Ka   Solid   20μ

Figure 9E. Electron probe Mn scan of the area shown in figure 9A.
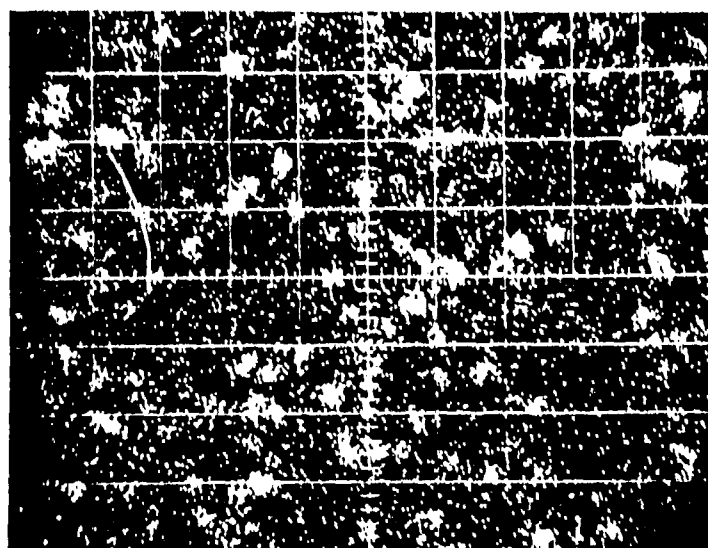
764   Scan   Fe Ka   Solid   20μ

Figure 9F. Electron probe Fe scan of the area shown in figure 9A.
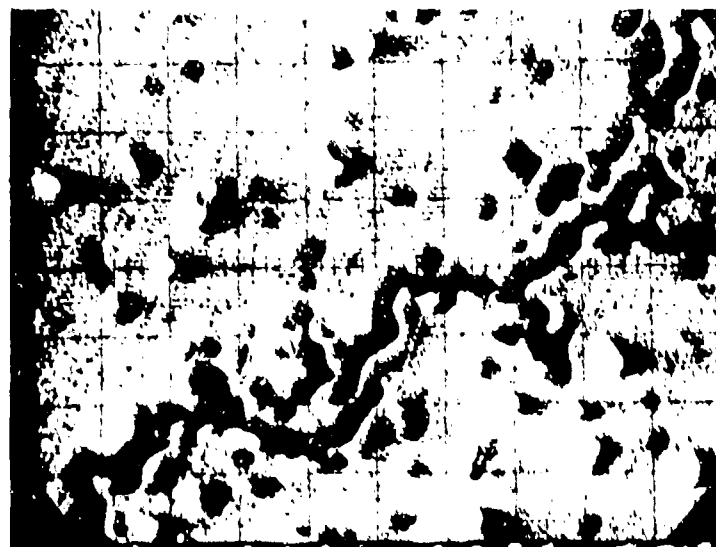
764 C1   Scan   12 Kv   10µ

Figure 10A. Electron probe sample current scan showing a linear defect on the surface at 100x.

764 C1   Scan   Al Kα   12 Kv   10µ

Figure 10B. Electron probe Al scan of the area shown in figure 10A.

16

764 C1   Scan   Mg Ka   12 Kv - 10µ

Figure 10C. Electron probe Mg scan of the area shown in figure 10A.

764 C1   Scan   Si Ka   12 Kv   10µ

Figure 10D. Electron probe Si scan of the area shown in figure 10A.

17
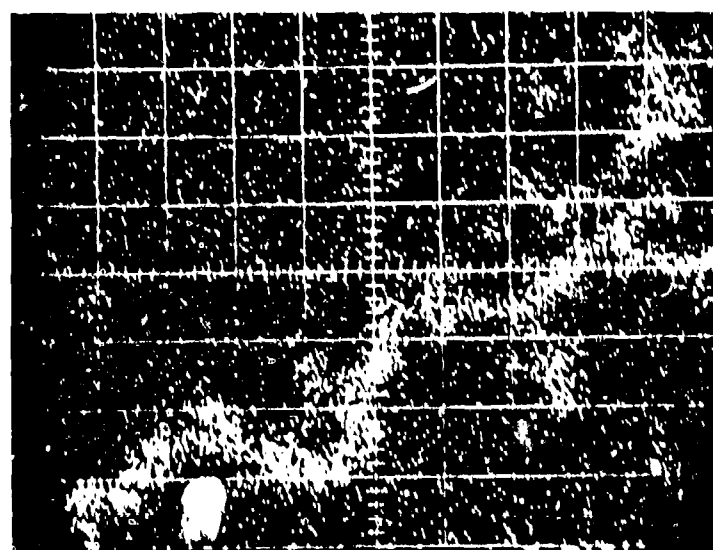
764 C1   Scan   O ka   12 kv   10μ

Figure 10E.   Electron probe O scan of the area shown in figure 10A.
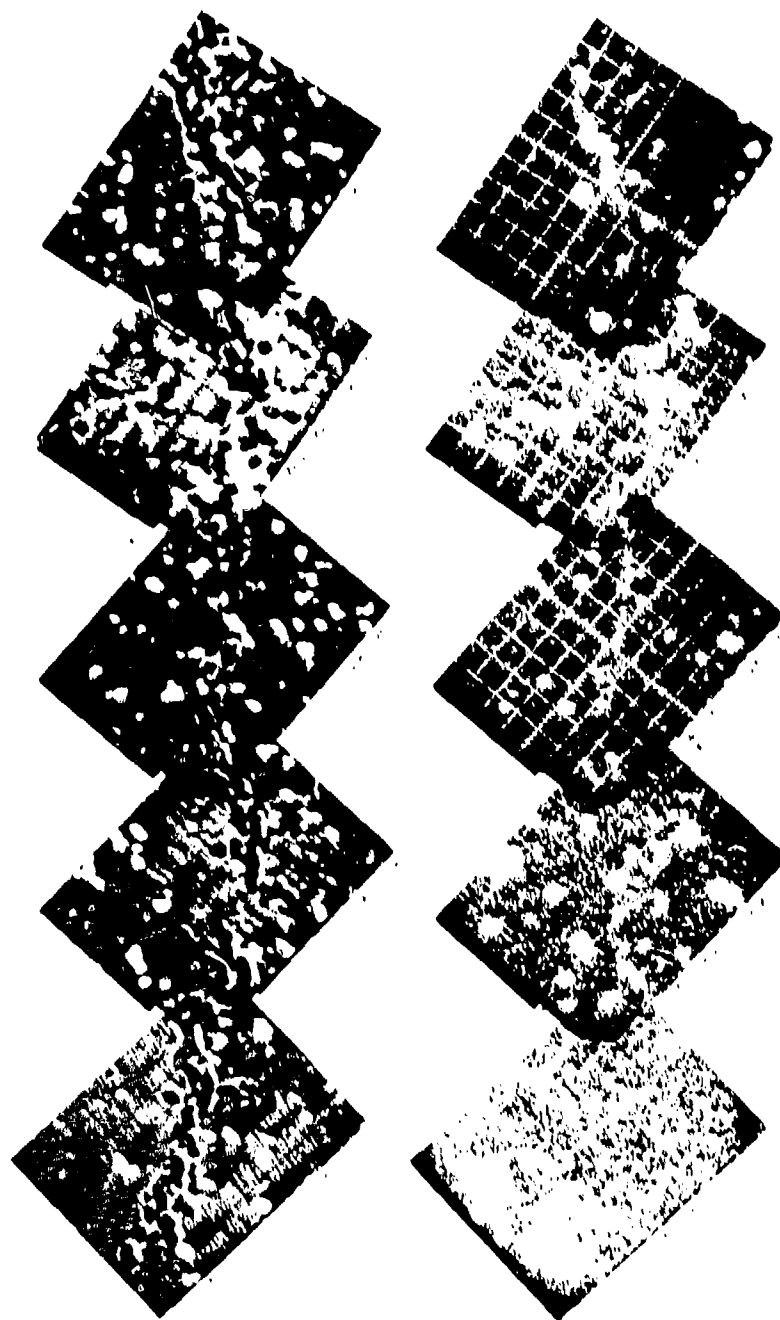
Figure 11. Electron probe current image scan and Mg scan showing a linear defect on the surface. The scans show approximately 43 μm of the defect.

photomicrographs of this are shown in figures 4B, 5B, 6B, and 7B)
obtained from above the bulkhead is similarly examined, and the results
shown in figures 12A-E and 13A-D. Figures 12A-E (1000x) again a
composite of sample current, Al, Mg, Si, and O, respectively, show a
bimodal distribution of particularly the Mg which is present as Mg_2Si
precipitates as well as distributed over the entire fracture surface.
Figures 13A-D (250x) show a similar high distribution of Si over the
fracture surface in areas other than the Mg_2Si precipitates. These
results, although qualitative, strongly infer an increased concentration
of Mg and Si over the fracture surface higher than that expected for
normal 6070-T6.

SUMMARY OF RESULTS

As discussed in the text, the failed fracture mode may coexist with
the normal fracture mode. Scanning electron micrographs show a greater
charging of the failed fracture surface than the normal fracture surface.
Furthermore, electron probe results show a higher concentration of Mg,
Si, and O on the failed fracture surface than on the normal fracture
surface. Oxygen is associated with the magnesium and silicon although
the magnesium and silicon do not necessarily coexist. This would be
consistent with the charging problems detected in the scanning electron
microscope.

During the billet pouring operation, if the billet is not properly
cooled, microcracks might form. The area in proximity to these cracks
would cool faster than the surrounding areas causing magnesium and
silicon to migrate to the crack. These microcracks would not be detected
when the billet is sliced into ingots due to their size. The ingot is next
placed in a gas furnace where it reaches a temperature of approximately
538°C. If the microcrack were on the face of the ingot, the magnesium
and silicon along the crack would be oxidized. If this crack were on the
"front" surface (the surface placed against the die) of the ingot, the
crack will be extruded with very little mixing, causing a portion of the
extrusion to be defective. If the crack were on the "rear" surface of the
ingot, sufficient mixing would occur during the extrusion process to
guarantee that the defect would not be continuous and, therefore, would
not affect the bulk properties of the finished product. If the crack were
not on the surface, but were contained within the ingot, no oxidation
would occur and sufficient mixing could take place to insure that the
high concentration of magnesium and silicon would be dispersed.

764 Fract   12 Kv   10μ

Figure 12A. Electron probe current image scan showing an abnormal
fracture surface at 1000x.
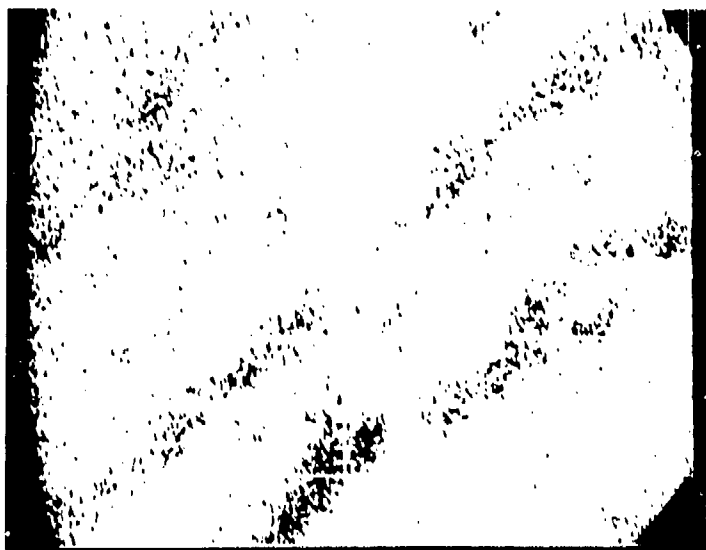
764   Fract   Scan   Al Ka   12 Kv   10μ

Figure 12B. Electron probe Al scan of the area shown in figure 12A.
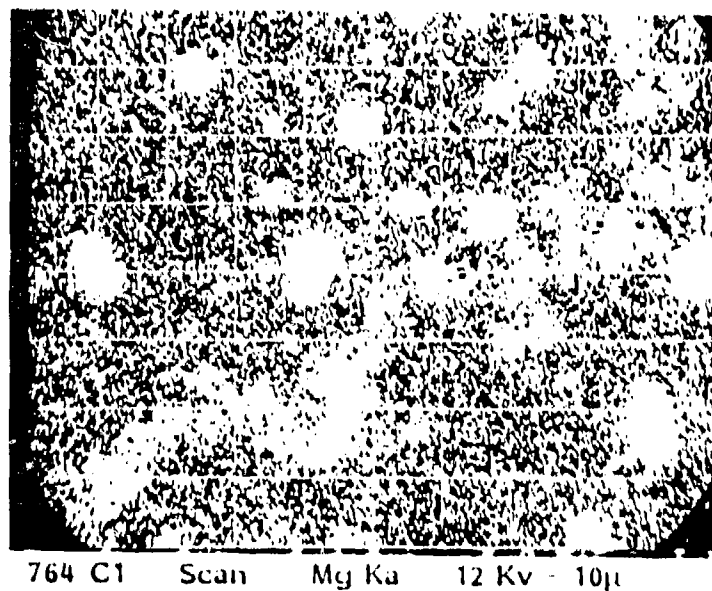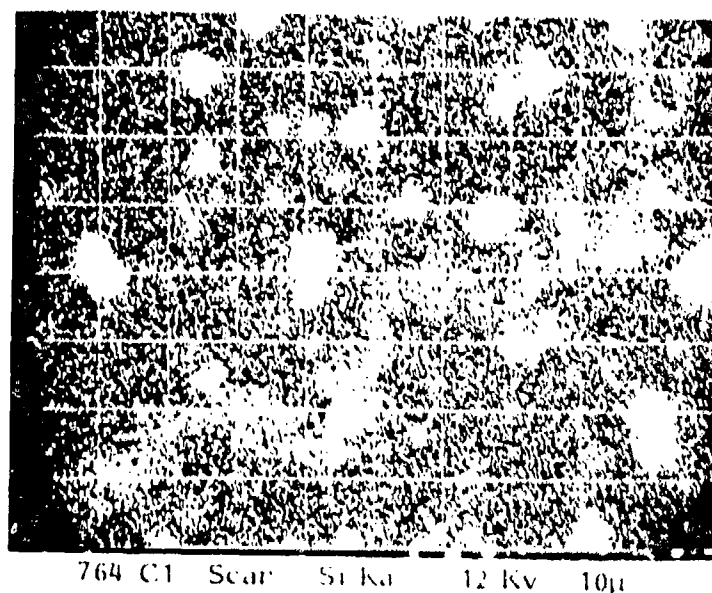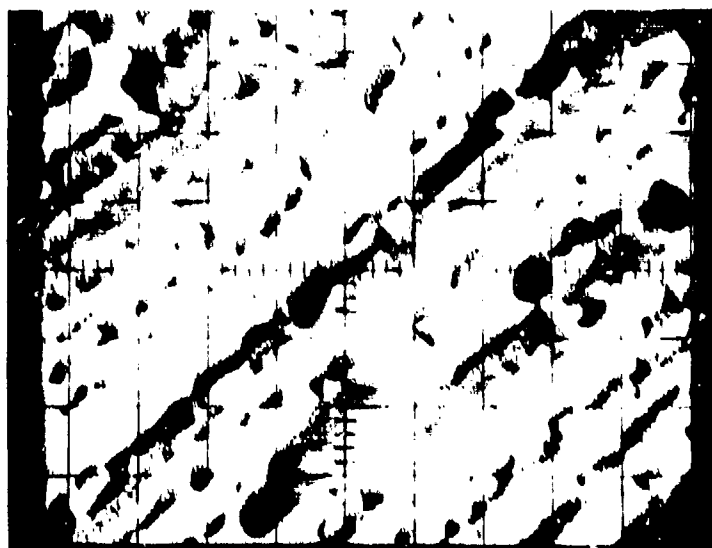
764 Fract Mg Ka 12 Kv 10μ

Figure 12C. Electron probe Mg scan of the area shown in figure 12A.

764 Fract Si Ka 12 Kv 10μ

Figure 12D. Electron probe Si scan of the area shown in figure 12A.

22
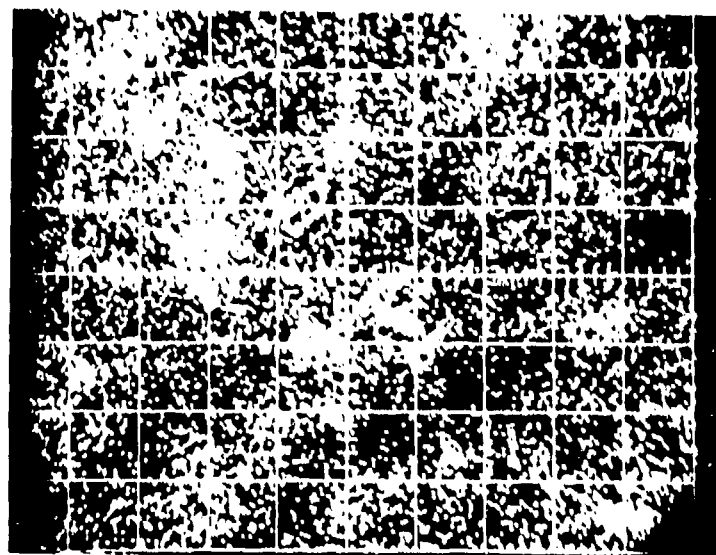
764 Fract   O Kα   12 Kv   10μ

Figure 12E. Electron probe O scan of the area shown in figure 12A.
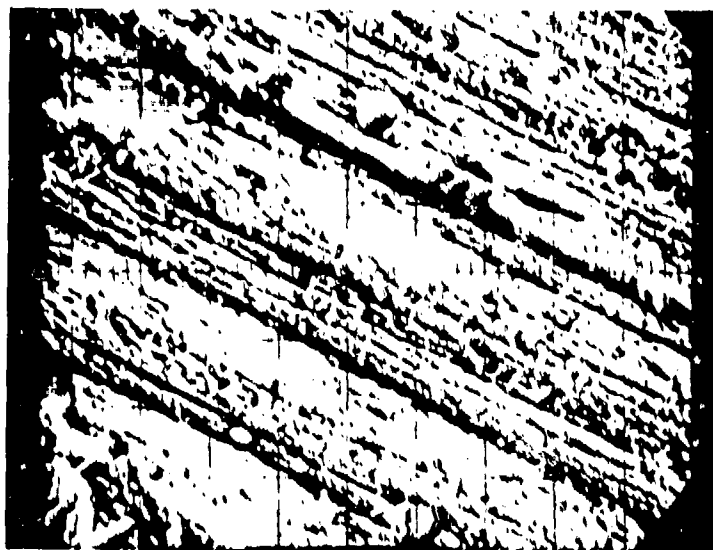
764   Fract A   Al Ka   12 Kv   40μ

Figure 13A. Electron probe current image scan showing an abnormal fracture
surface at 250x.
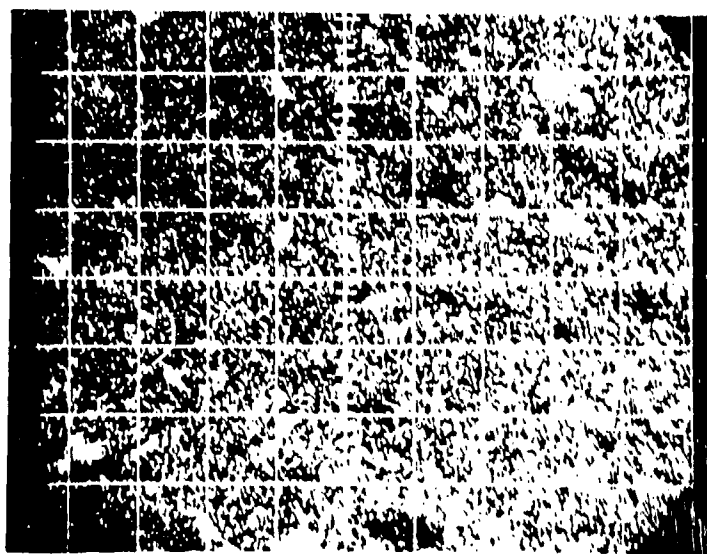
764 Fract A   Si Ka   12 Kv   40μ

Figure 13B. Electron probe Si scan of the area shown in figure 13A.
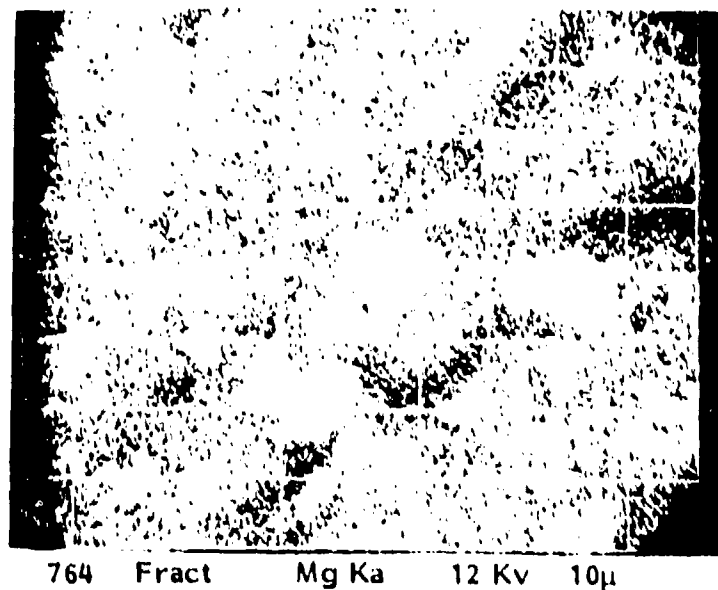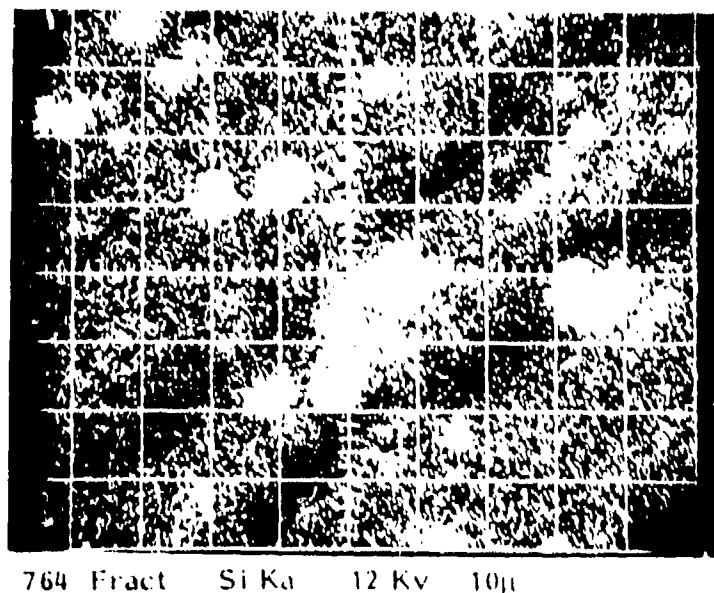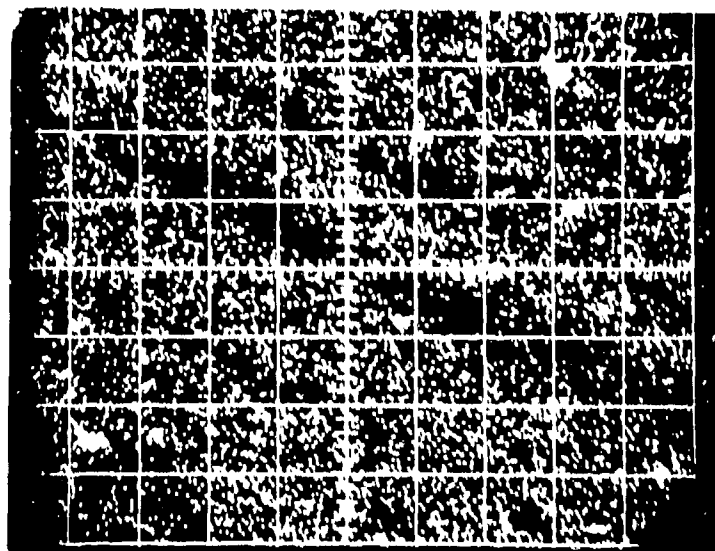
764 Fract A Mg Ka 12 Kv 40μ

Figure 13C. Electron probe Mg scan of the area shown in figure 13A.
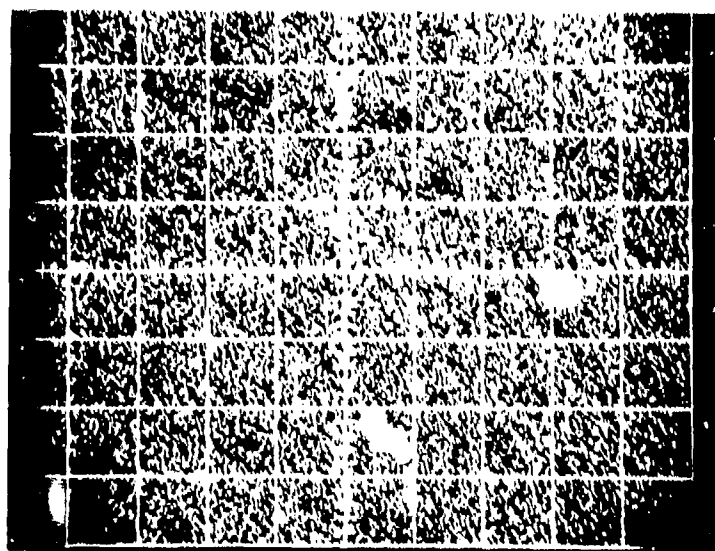
764 Fract A Al Ka 12 Kv 40μ

Figure 13D. Electron probe Al scan of the area shown in figure 13A.

25

RECOMMENDATIONS

Screening techniques applied either at the billet sectioning stage, the extrusion stage, or the final screening stage could be employed to eliminate defective fins from the final lots. A dye-penetrant visual examination of the ingots prior to extrusion could be employed to detect cracking on the front face of the billet surface; however, this technique would require that the ingot be machined and polished to insure that microcracks are not hidden by smearing of material. Furthermore, the technique would be time consuming and expensive.

A flow pattern study of an extruded length of the XM27 fin could be performed to determine the optimum length of fin to be removed from the front surface of the extruded section. This study would determine where sufficient mixing has occurred to insure that any microcracks present in the billet would not affect the bulk properties of the final piece. Although this process would insure against future failures of the type discussed, many good fins would be eliminated by the cropping.

Prior to machining the fins, hydrostatic testing or mandrel testing could be employed for a 100% screen, and thereby guarantee that the properties of the fin section will meet the necessary requirements.

26

APPENDIX

EXPLANATION OF ELECTRON MICROPROBE SCANS

Scanning electron probe images are used in this report to document the chemical nature of the subject aluminum alloy fracture surfaces. The following section describes the techniques by which such images are obtained.

In the electron probe, a focused electron beam (spot size 0.5 μm) is allowed to impinge on a sample surface. Of the many interactions which occur between the beam and the sample, those of primary interest are electron backscattering, the generation of target or sample current, and the production of x-rays. The number of backscattered electrons is proportional to the mean atomic number of the area being excited by the electron beam. A scintillator, light-pipe, photomultiplier tube combination is used to detect the backscattered electron signal. Target current or sample current is essentially the inverse of the backscattered electron signal, consisting primarily of electrons which are not backscattered, but rather which are absorbed in the sample. Target current is read out through a microammeter to ground. Both target current and backscattered electron signals may be employed conveniently for imaging of the sample, being sensitive both to compositional variation and to topographic details at the sample surface.

X-rays generated in the sample by the impinging electron beam have wavelengths (or energies) which are characteristic of the element(s) being excited and intensities proportional to the amount of the element(s) present. X-ray spectrometers are provided which permit the identification of all elements heavier than $Z = 8$ present in the sample. When quantitative analysis is required, the electron probe is normally operated in the static mode in which the electron beam is not moved, the point of interest on the sample being positioned under the focused electron beam. For qualitative analysis, the probe is commonly operated in the scanning mode. In this technique, the focused electron beam is scanned across the specimen by means of electrostatic coils or deflection plates producing a raster on the surface while a scan raster is simultaneously produced on the cathode ray tube (CRT) of an oscilloscope. Any signal generated by the scanning electron beam, e.g., the x-ray signal from one of the elements present in the sample, target current, or backscattered electron signal may then be used to modulate the brightness of the oscilloscope and, thus, produce a two-dimensional image showing the distribution of that element or sample current variation across the

27

sample surface. The magnification of the image is determined by the size ratio between the raster on the specimen and the raster on the monitor CRT. If the same area is sequentially scanned, for each exposure the x-ray spectrometers are reset for each of the elements present, element images are obtained which can be used to compare similarities and differences in element distribution.

In order to illustrate how such techniques may be employed for imaging purposes, a sample consisting of a 200 mesh copper electron microscope grid superimposed over a 1000 mesh silver screen, both mounted on a brass holder, is examined. Figure A1 is a reverse sample current image of the grid/screen combination at 250x magnification. Note the extensive topographic detail visible on the upper, copper grid, and also that the silver screen is somewhat brighter than the copper. Figure A2 is of the same area as figure A1, but a signal from an x-ray spectrometer set at the appropriate Bragg Angle for CuK_α radiation was used to intensity-modulate the CRT. Copper present inside the 1000 mesh silver screen is due to the brass pin on which the grids are mounted. Finally, figure A3, again of the identical area and the same magnification, is obtained using the current of a detector set to diffract AgL_α radiation; the silver bars of the 1000 mesh screen are clearly displayed.
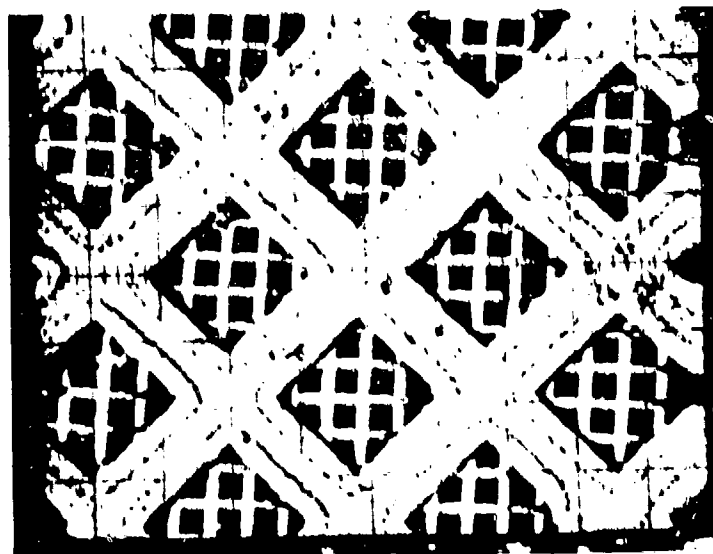
Figure A1. Electron probe current image scan of a 200 mesh copper electron microscope grid superimposed over a 1000 mesh silver screen.
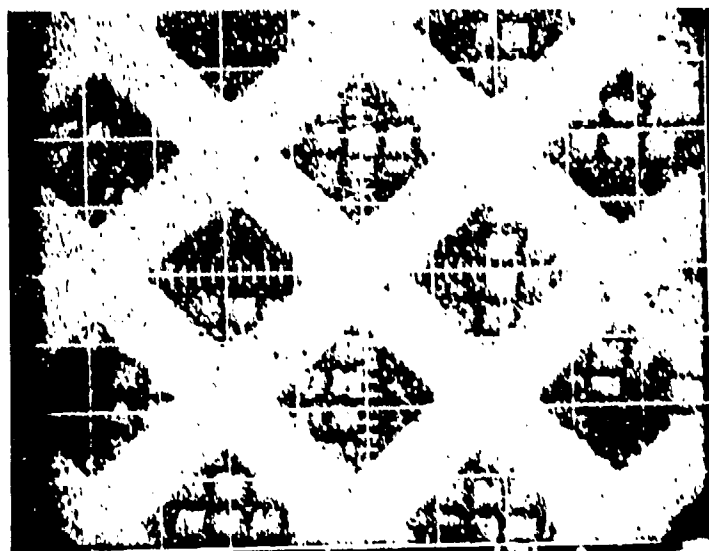
Figure A2. Electron probe Cu scan of the area shown in figure A1.
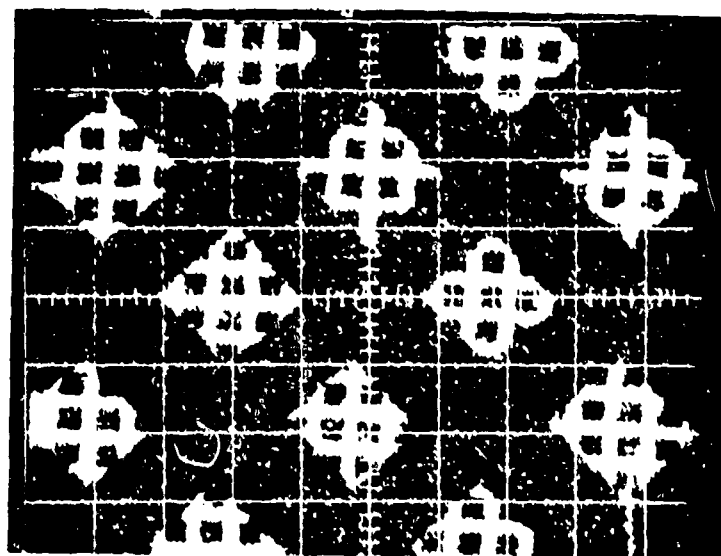
Figure A3. Electron probe Ag scan of the area shown in figure A1.

DISTRIBUTION LIST

Commander
US Army Armament Research & Development Command
ATTN: DRDAR-LCU-D-I   (5)
        DRDAR-Q/R
        DRDAR-LCU-TB   (3)
        DRDAR-TSS   (5)
        DRDAR-LCB-M   (2)
        DRDAR-LCA   (10)
Dover, NJ 07801

Commander
US Army Test & Evaluation Command
ATTN: DRSTE-CM-F   (2)
        DRSTE-SG-H   (1)
Aberdeen Proving Ground, MD 21005

Commander
US Army Materiel Development & Readiness Command
ATTN: DRCDE-D   (2)
        DRCDE-R
        DRCQA-P
        DRCSF
        DRCDE-A   (12)
Alexandria, VA 22333

Commander
US Army Armament Readiness Command
ATTN: DRSAR-LEP   (10)
        DRSAR-ASF
Rock Island, IL 61201

Commander
US Army Training & Doctrine Command
ATTN: TRADOC Liaison Officer, TECOM   (5)
Aberdeen Proving Ground, MD 21005

Commander
US Army Logistics Evaluation Agency
ATTN: DALO-LEI-W
New Cumberland Army Depot
New Cumberland, PA 17070

Commander
US Army Operational Test & Evaluation Agency
ATTN: CSTE-TEM-IN
5600 Columbia Pike
Falls Church, VA 22041

Commander
US Army Training & Doctrine Command
ATTN: ATCD-CM I
        ATCD-PM
        ATCD-TM
Fort Monroe, VA 23651

Commander
US Army Combined Arms Combat Developments Activity
ATTN: ATCA-CCM
Fort Leavenworth, KS 66027

Commander
US Army Environmental Health Agency
Aberdeen Proving Ground, MD 21010

Commander
US Army Matinenance Management Center
ATTN: DRXMD-MEV (2)
Lexington, KY 40507

Commander
US Army Cold Regions Test Center
APO Seattle 98733

Commander
US Army Yuma Proving Ground
Yuma, AZ 85364

Commander
Harry Diamond Laboratories (2)
2800 Powder Mill Road
Adelphia, MD 20783

Commander
US Army TRADOC Combined Arms Test Activity
ATTN: ATCAT-OP
Fort Hood, TX 76544

Commander
US Army Forces Command
ATTN: AFOP-RE
Fort McPherson, GA 30330

Commander
Military Traffic Management Command
ATTN: MT-SA
Washington, DC 20315

Commander
US Army Logistics Center
ATTN: ATCL-MM (2)
Fort Lee, VA 23801

Commander
TRADOC System Analysis Agency
ATTN: AATA-TRA
White Sands Missile Range
White Sands, MN 88002

Commander
US Army Combat Developments Activity (Alaska)
ATTN: ATCA-AL
APO Seattle, WA 98749

Commander
US Army Natick Research & Development Command
ATTN: DRXNM-USA
Natick, MA 01760

Commander
US Army Transportation Engineering Agency
ATTN: MTT-TG
Military Traffic Management & Terminal Service
PO Box 6276
Newport News, VA 23606

Commander
US Army Ordnance Center & School
Aberdeen Proving Ground, MD 21005

Commander
US Army Infantry Center
ATTN: ATZB-CD-MS-F
Fort Benning, GA 31905

Commander
Air Force Systems Command
ATTN: APSC-CST
Andrews Air Force Base, MD 20331

Headquarters
Department of the Army
ATTN: DAEN-ZB
        DASG-HCL
Washington, DC 20314

Headquarters
Department of the Army
ATTN: DAPC-PMO
Alexandria, VA 22331

Commander
US Army Concepts Analysis Agency
ATTN: CAA MOCA-PP
8120 Woodmont Avenue
Bethesda, MD 20014

Project Manager
Training Devices
ATTN: DRCPM-TND
Fort Benning, GA 31905

Headquarters
Department of the Army
ATTN: SARD
        SAIL
        DACS-ZB
        DAMA-WSW   (2)
        DAMO-RQD   (2)
        DALO-ZB
        DACA-ZB
        DAAG-ZB
        DAMI-ZB
        DAPE-ZB
        DAIG-ZB
        DALO-SMM-E
        DAMO-ZD
        UNSEC (OR)
        SAUS-OR
        DAMO-FD
Washington, DC 20310

Project Manager
Munitions Production Base Modernization & Expansion
ATTN: DRCPM-PBM   (2)
Dover, NJ 07801

Project Manager
Mortar/Artillery Locating Radars
ATTN: DRCPM-MALR
Fort Monmouth, NJ 07703

Commandant
US Army Armor School
ATTN: ATSB-CD-MM
Fort Knox, KY 40121

Commandant
US Army Quartermaster School
Fort Lee, VA 23801

Commandant
US Army Missile & Munitions School
ATTN: ATSK-CTD
Huntsville, AL 34809

Commandant
US Marine Corps
Code RD&S   (2)
Headquarters Marine Corps
Washington, DC 20380

Commandant
US Army Infantry School
ATTN: ATSH-I
Fort Benning, GA 31905

President
US Army Infantry Board
Fort Benning, GA 31905

Director
US Army Materiel Systems Analysis Activity
ATTN: DRXSY-RE   (2)
        DRXSY-GI   (2)
Aberdeen Proving Ground, MD 21005

Director
US Army Ballistics Research Laboratories
ATTN: DRXBR-X   (2)
        DRXBR-XA-LB   (2)
Aberdeen Proving Ground, MD 21005

Director
US Army Human Engineering Laboratory
Aberdeen Proving Ground, MD 21005

Director
Marine Corps Development & Education Command   (2)
Quantico, VA 22134

Director
DARCOM Field Safety Activity
ATTN: DRXOS-ES
Charlestown, IN 47111

Mortar Committee
ATTN: ATSH-W-MO
Fort Benning, GA 31905

US Marine Corps Liaison Officer
US Army Test & Evaluation Command
Aberdeen Proving Ground, MD 21005

Commander
US Army Aberdeen Proving Ground
ATTN: STEAP-MT-A   (6)
        STEAP-MT-G
        STEAP-MT-O
        STEAP-MT-T, Mr. Lambert
        STEAP-MT-X
        STEAP-SA
Aberdeen Proving Ground, MD 21005

Defense Documentation Center
ATTN: Document Service Center
Cameron Station
Alexandria, VA 22314

Commander
US Air Force Test & Evaluation Command
ATTN: AFTC/TE
Kirtland, AFB, NM 87115

Commander
Operational Test & Evaluation Force
US Naval Base
Norfolk, VA 23511